nature physics

ARTICLES

https://doi.org/10.1038/s41567-018-0103-2

Attosecond coupled electron and nuclear dynamics in dissociative ionization of H_2

L. Cattaneo[1*], J. Vos[1], R. Y. Bello[2], A. Palacios[2,3], S. Heuser[1], L. Pedrelli[1], M. Lucchini[1,7], C. Cirelli[1,4], F. Martín[2,5,6] and U. Keller[1]

The interaction of an extreme-ultraviolet attosecond pulse with a molecular system suddenly removes electrons, which can lead to significant changes in the chemical bonding and hence to rearrangements of the residual molecular cation. The timescales of the electronic and nuclear dynamics are usually very different, thus supporting separate treatment. However, when light nuclei are involved, as in most organic and biological molecules containing atomic hydrogen, the correlation between electronic and nuclear motion cannot be ignored. Using an advanced attosecond pump–probe spectroscopic method, we show that the coupling between electronic and nuclear motion in H_2 leaves a clear trace in the phase of the entangled electron–nuclear wave packet. This requires us to re-evaluate the physical meaning of the measured phase, which depends on the energy distribution between electrons and nuclei. The conclusions are supported by ab initio calculations that explicitly account for the coupling between electronic and nuclear dynamics.

Light is increasingly being harnessed to investigate ultrafast and microscopic phenomena in many fields. However light-driven processes in life sciences, physics and engineering are often not fully understood. Only recently with the advent of attosecond science[1,2] could light-induced electron dynamics be investigated in real time, well separated from the slower nuclear dynamics that typically range from tens to hundreds of femtoseconds and even longer. Novel attosecond measurements have been used to resolve dynamics of primary ionization processes in atoms, such as tunnel ionization[3] and photoemission[4]. These pioneering measurements triggered more theoretical and experimental activities in atomic targets[5–12], and there is a strong interest in expanding these efforts to more complex systems such as molecules[13–18] and condensed matter[19,20].

Here we address a fundamental challenge for molecules composed of light atomic species, such as atomic hydrogen: to time resolve the coupled electron–nuclear dynamics occurring in such systems. For this we have combined experimental measurements with complete ab initio theoretical calculations to investigate these complex dynamics in the simplest of all molecules containing light nuclei, H_2 (refs [21–25]). We used the reconstruction of attosecond beating by interference of two-photon transitions (RABBITT) technique[26], based on the combination of an extreme-ultraviolet (XUV) attosecond pulse train (APT)[27] with a time delayed, long and rather weak infrared (IR) pulse. This technique has proved to be one of the most reliable[12] and established methods for the investigation of photoionization time delays in atoms[5,7,8,12], even in the presence of double ionization processes[6], spin–orbit interaction[10] and resonances[9,13,16]. However, applications of RABBITT to molecules are very scarce.

In particular, Haessler and co-workers measured the phase of the electron wave packet released on photoionization in a molecular target: N_2 (ref. [13]). In particular, they observed the distinct influence of complex resonances in the continuum for different vibrational states of N_2^+. Recently Huppert et al.[16] performed a similar study that accessed the photoionization time delay induced by shape resonances in N_2O and H_2O. However, none of these studies gave access to coupled nuclear–electronic dynamics in those molecules. To do so requires not only subfemtosecond time resolution, but also the coincidence detection of both the ejected electrons and the residual charged molecular ions. This is very challenging, as (1) the coincidence detection requires an overall low count rate to avoid false coincidence between the ejected electrons and ions, and (2) the access to angular-resolved data, if no molecular alignment is used, relies only on dissociative ionization, usually associated with very low yields compared with non-dissociative ionization (see Supplementary Information).

In the present study, we meet these requirements by combining the RABBITT technique with our AttoCOLTRIMS apparatus consisting of a cold target recoil ion momentum spectroscopy (COLTRIMS) allowing for full three-dimensional (3D) coincidence detection[28–30]. To visualize the entangled electron–nuclear dynamics, we ionized randomly oriented H_2 molecules in the energy region where molecular autoionization manifests itself upon population of doubly excited states (DESs)[31–33]. We show, in fact, that the phase of the electron wave packet can be strongly influenced by the existence of resonances embedded in the continua[9,13,16], and can carry the imprint of specific nuclear dynamics. This calls for a new interpretation of the spectral phases extracted from RABBITT experiments, as nuclei can no longer be considered as frozen entities, but as active players during the photoionization process. The entire analysis of the presented experimental data is supported by a theoretical approach that accurately incorporates both the electronic and nuclear motions and their correlation[34].

Within the axial recoil approximation[35] we reconstruct the H_2^+ molecular axis before dissociation, as shown in Fig. 1a,b, and define the angle of its axis with respect to the XUV polarization axis: the β angle (see Supplementary equation (2)).

[1]Physics Department, ETH Zurich, Zurich, Switzerland. [2]Departamento de Química, Módulo 13, Universidad Autónoma de Madrid, Madrid, Spain. [3]Institute for Advanced Research in Chemical Sciences (IAdChem), Universidad Autónoma de Madrid, Madrid, Spain. [4]Empa – Swiss Federal Laboratories for Materials Science and Technology, Dübendorf, Switzerland. [5]Instituto Madrileño de Estudios Avanzados en Nanociencia (IMDEA-Nanociencia), Madrid, Spain. [6]Condensed Matter Physics Center (IFIMAC), Universidad Autónoma de Madrid, Madrid, Spain. [7]Present address: Department of Physics, Politecnico di Milano, Milano, Italy. *e-mail: claura@phys.ethz.ch

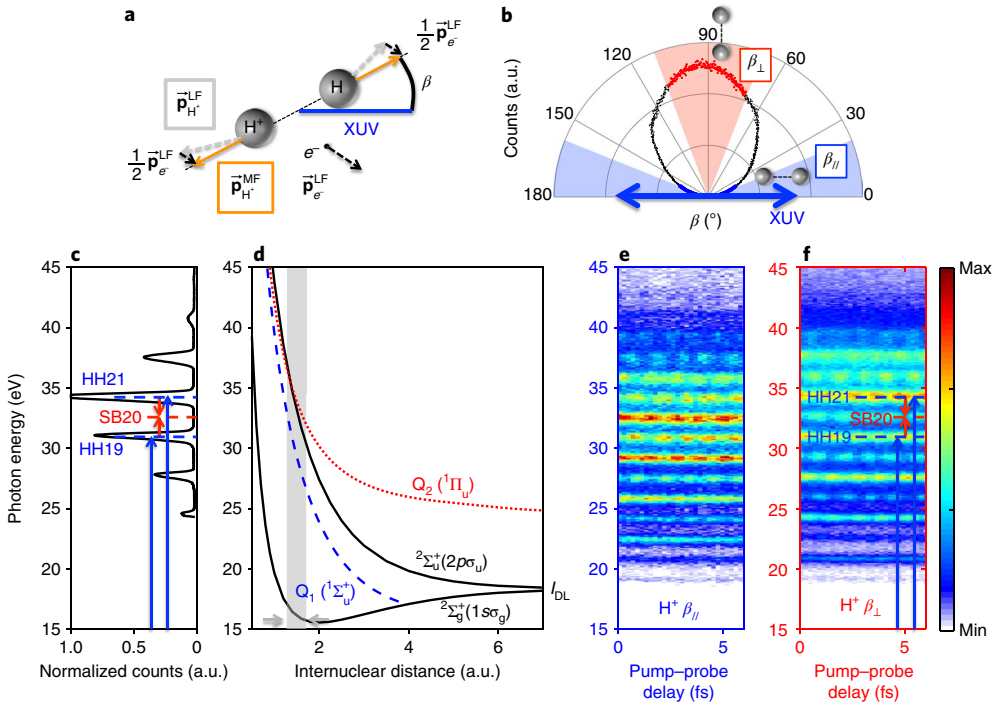

Fig. 1 | H_2 dissociative photoionization. a, Ion momenta vectors $\mathbf{p}_{H+}$ and $\mathbf{p}_{H}$, in the laboratory frame (LF, grey dashed arrows) and in the molecular frame (MF, orange solid arrows). $\mathbf{p}_{e-}$ is the electron momentum vector. **b**, Polar plot of H^+ counts as a function of β: $\beta_\perp = 70$–$110°$ (red cone) and $\beta_{//} = 0$–$20°$ and 160–180° (blue cones). The integration cone of ±20° is a compromise between reasonable experimental statistics and good comparison with theory, which assumes perfect parallel orientation. **c**, XUV spectrum. **d**, Relevant potential energy curves as a function of the internuclear distance; the grey area represents the Franck–Condon region. **e**,**f**, RABBITT traces of photoelectrons in coincidence with H^+ by selecting $\beta_{//}$ (**e**) and $\beta_\perp$ (**f**). In **c** and **f**, the blue and red arrows indicate the absorption of an XUV photon (blue arrows) and the absorption/emission of an IR photon (red arrows).

The energy conservation involved in the dissociative ionization of H_2 on absorbing a single XUV photon of energy E_{XUV} can be expressed as $E_{XUV} = KER + E_{kin}^{e^-} + I_{DL}$, where $E_{kin}^{e^-}$ is the electron kinetic energy, $KER = E_{kin}^{H^+} + E_{kin}^{H}$ is the kinetic energy released by the nuclear part during dissociation (see Supplementary equation (3)) and I_{DL} is the dissociation limit of the molecular ion at 18.078 eV (Fig. 1d). In our experiments, due to the energy range 24–42 eV of the interacting XUV photons (Fig. 1c) and the randomly oriented molecules (Fig. 1b), several ionization paths can be activated while leading to the same I_{DL} (refs [14,36]).

We observe direct ionization populating the cationic ground state $^2\Sigma_g^+(1s\sigma_g)$ for $E_{XUV} < \sim 25$ eV, resulting in molecular fragments with a KER within approximately 1 eV, and the first excited state of the ion $^2\Sigma_u^+(2p\sigma_u)$ for $E_{XUV} > \sim 30$ eV and KER 10–12 eV (black solid potential curves in Fig. 1d). Owing to the low intensity of the 25th and 27th harmonics, no contribution from higher ionic states, as, for example, the $^2\Pi_u(2p\pi_u)$ or the $^2\Sigma_g(2s\sigma_g)$ state, is observed in the spectrum.

Moreover, we also populate the first two DES series, Q_1 and Q_2, for molecules preferentially oriented parallel and perpendicular with respect to the XUV polarization axis, respectively (see Methods). These states autoionize to the previously mentioned, ground and first excited ionic states, but result in higher energetic ionic fragments compared with the relative direct path. Figure 1d shows only the lowest-lying states for both DES series, that is, $Q_1{}^1\Sigma_u^+$ (blue dashed line) and $Q_2{}^1\Pi_u$ (red dotted line), as their contribution strongly dominates over all the others.

The experimental outcome of parallel oriented molecules is directly compared with calculations performed by solving the time-dependent Schrödinger equation employing a basis of states that accurately describe molecular autoionization and the electron–nuclear couplings, that is, going beyond the usual adiabatic approximation in which electron dynamics precedes any nuclear rearrangement[34]. In short, we performed a multichannel close-coupling expansion of the electronic continua associated with the two lowest ionic states ($^2\Sigma_g^+(1s\sigma_g)$ and $^2\Sigma_u^+(2p\sigma_u)$) and the first two series of DES (Q_1 and Q_2). Only molecular states of $^1\Sigma_g^+$ or $^1\Sigma_u^+$ total symmetry were considered, thus restricting the outcome of our calculations to the case of collinear pump and probe fields interacting with H_2 molecules aligned parallel to the polarization direction (see Supplementary Information). As calculations for the perpendicular orientation of the molecule in the context of RABBITT experiments are prohibitively expensive, the comparison is only possible for the data retrieved for the parallel orientation.

We can separate the two paths leading towards the lowest $Q_1{}^1\Sigma_u^+$ and $Q_2{}^1\Pi_u$ DESs by selecting the two different molecular orientations, $\beta_{//}$ and $\beta_\perp$ (see β angle in Fig. 1a,b and Supplementary equation (2)), and extract the associated KER. The symmetry-selected KER spectrum, in turn, will enable us to disentangle direct ionization and autoionizing pathways[37,38]. Sanchez and Martín[37] assigned the different peaks observed in the KER spectrum for the $^1\Sigma_u$ final symmetry and photon energy of 27 eV, separating the non-resonant from the resonant contributions, as reproduced in Fig. 2a. As can be clearly observed, the non-resonant cross-section, or direct ionization curve (yellow curve in Fig. 2a) has an influence only within the first couple of electronvolts along the KER axis. Conversely, the resonant contribution, or autoionization curve (red curve in Fig. 2a), presents a significant cross-section over a broad range of energies. Note that above 2 eV, the resonant term is the only contribution to the total cross-section, thus making the KER of the ion fragments a valid tool to disentangle direct from autoionizing paths in the dissociative ionization of H_2.

This separation is nicely reproduced in the experimental data (Fig. 2e,f). Figure 2b,e,f shows the time-integrated dissociative ionization probability as a function of the KER and electron kinetic

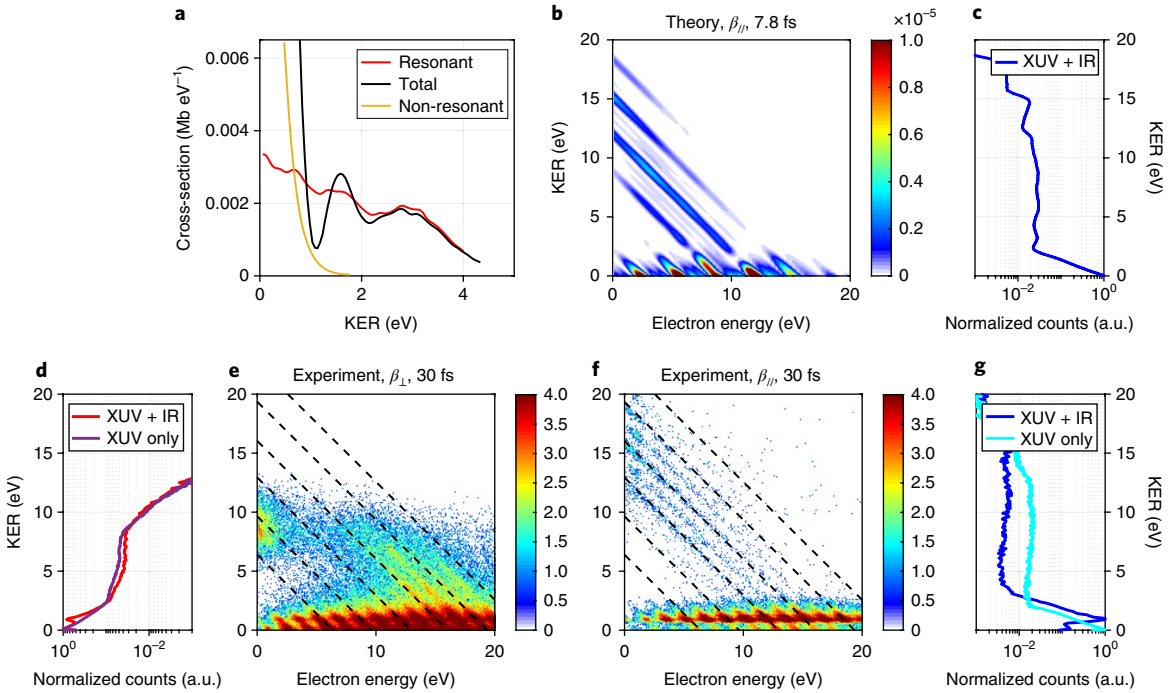

Fig. 2 | Cross-section and kinetic energy correlation diagrams. a, Calculated cross-section for the H_2 molecule, at 27 eV photon energy, considering the resonant (red), the non-resonant (yellow) and the total contributing paths (black) as a function of the proton (H^+) kinetic energy. Panel adapted from ref. [37], APS. **b**,**e**,**f**, Theoretical calculation corresponding to the total ionization for the parallel orientation (**b**) and experimental results for $\beta_{\perp}$ (**e**) and $\beta_{//}$ (**f**). Colour bar in logarithmic scale. Black dashed lines highlight the HH positions. **c**,**d**,**g**, KER spectra integrated over all electron kinetic energies, corresponding to **b**, **e** and **f**, respectively. In addition, **d** and **g** show the XUV-only case (purple and cyan curves, respectively). In $\beta_{//}$, the HHs populate the $^1\Sigma_u^+$ final symmetry of the two-electron target, resulting in one electron in the $^2\Sigma_g^+(1s\sigma_g)$ ($^2\Sigma_u^+(2p\sigma_u)$) ground state of the ion and the second electron in the continua with odd (even) angular momenta, respectively. The SBs, instead, populate the $^1\Sigma_g^+$ final symmetry with the same states of the ion but with different odd/even electron angular momentum.

energy when both XUV and IR fields are present. In other words, for each dissociative event, these 2D plots show how the energy ($E_{XUV} - I_{DL}$) redistributes between the electron and the coincident ion fragments $H^+ + H$.

In all of these 2D plots, two distinct KER regions are clearly visible: the first one between 0 and roughly 1.5 eV, and the second one above 1.5 eV. In the low-KER region, the non-resonant or direct photoionization path is the dominant contribution, specifically from the $^2\Sigma_g^+(1s\sigma_g)$, although weakly modulated by a coherent resonant component[39] (Fig. 2a). In contrast, the resonant or autoionizing contribution is almost entirely responsible for the KER signal appearing above 1.5 eV. The direct photoionization to $^2\Sigma_u^+(2p\sigma_u)$ opens only for photon energies $E_{XUV} > \sim 30$ eV, thus resulting in ion fragments with KER > 10 eV.

Figure 2b represents the energy correlation for the theoretical case only including the parallel configuration, that is, only the $^1\Sigma_u^+$ is allowed by the one-photon XUV absorption (see Methods). For the simulations, we chose a relatively short IR pulse (7.8 fs) to avoid unphysical reflections of the ejected electron from the box boundaries (see Supplementary Information).

Figure 2e,f shows the experimental case for the two molecular orientations: $\beta_{\perp}$ perpendicular and $\beta_{//}$ parallel, as defined in Fig. 1b. The lateral panels, namely Fig. 2c,d,g, present the KER spectra integrated over all electron kinetic energies associated with the 2D plots in Fig. 2b,e,f, respectively.

The signal corresponding to the XUV single-photon absorption, also named high harmonics (HHs), appears as a strong signal compared with the XUV + IR two-photon absorption signal or sidebands (SBs). This is clearly visible in Fig. 2b (theory) while in the experimental measurements (Fig. 2e,f), the HH positions are highlighted with black dashed lines. The differences in intensity between the calculated and the measured SB signals are probably due to the different duration of the theoretical and experimental IR pulses. We found an overall very good agreement between theory (Fig. 2b,c) and experiment (Fig. 2f,g, blue curve) for the $\beta_{//}$ case.

However, the use of a different IR pulse length in the theory and experimental measurements (~30 fs) leads to a visible discrepancy for nuclear fragments in the low-KER region. Indeed, Fig. 2d–g present a double peak profile in the low-KER region, not visible in the theoretical calculations (Fig. 2b,c) nor in the XUV-only absorption case for $\beta_{\perp}$ and $\beta_{//}$ (purple and cyan dashed curves in Fig. 2d,g, respectively). This is a clear indication that the long-IR field used in the experiments plays an active role during the evolution of the fragmentation process, an effect commonly referred to as bond softening. Even moderately intense fields, as in our case (1.4×10^{11}–3.0×10^{11} W cm^{-2}, see Supplementary Fig. 2), can dress the potential energy curves and allow alternative fragmentation channels for certain vibrational states to open, resulting in ion fragments with slightly higher energy around 1 eV (refs [40–42]). The shorter pulses employed for the theoretical simulations prevent the appearance of the bond-softening signal at low KER. As the KER increases, where autoionization occurs, theory and experiment converge towards a better agreement.

The photoelectron–photoion spectra can be analysed as a function of the time delay to extract the phase of the molecular wave packet, by exploiting the RABBITT technique (see Fig. 1e,f). Two-photon transitions (blue and red arrows in Fig. 1c,e) are induced in the target gas by the interaction of a XUV APT (Fig. 1c) phase-locked with the generating field and the probing IR field itself (see Methods).

This will produce a photoelectron spectrum that peaks not only at energies corresponding to the odd HHs, $HH_{2q\pm1}$ (q is an integer

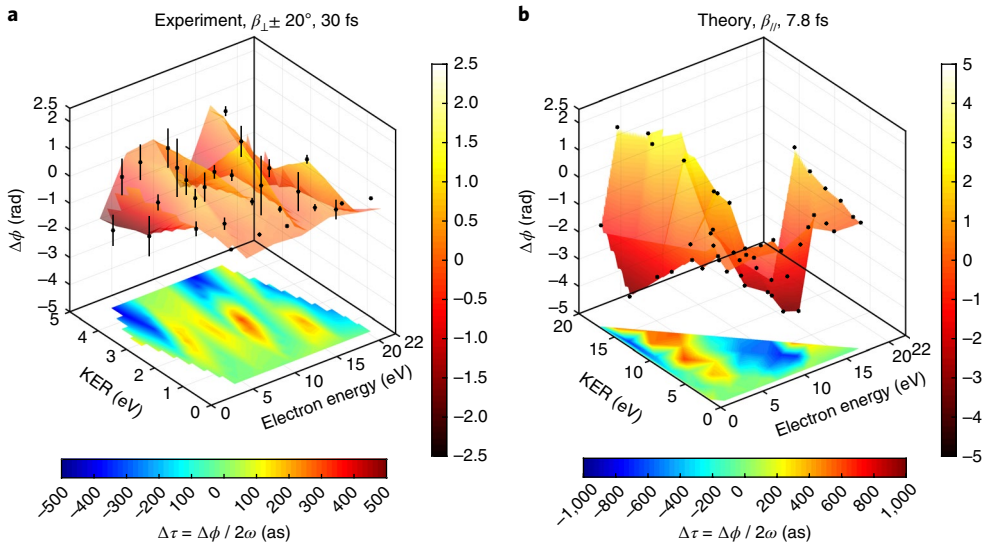

Fig. 3 | 3D nuclear–electron phase–time map. a, Extracted experimental phases (3D surface) and corresponding time delay (2D projection at the bottom) for $\beta_\perp$ as a function of both KER and electron energy. Phases and time delays are expressed with two different colour bars. The KER upper limit is 5 eV subdivided in intervals of 1 eV, due to statistical limitations. The electron energy upper limit is 22 eV sampled every 3.2 eV using an integration range around each SB maximum of ±0.35 eV. **b**, Ab initio calculations accounting for all electron–electron and nuclear–electron interaction terms for the $\beta_{//}$ configuration. The KER upper limit is 20 eV subdivided in KER intervals of 1 eV. Each surface is a linear interpolation between the data points (black solid circles). In the experimental case, each data point represents the weighted mean over a set of eight independent measurements with corresponding error bars (vertical black lines) considering two terms: the statistical standard deviation over all independent measurements and the average uncertainty of each SB fit as reported in ref. [12].

number), but also at the SB position of order $2q$, SB_{2q} (red arrows in Fig. 1c,f).

The ionization amplitude visible in each SB (Fig. 1e,f) is governed by the interference between quantum paths, which can be expressed as follows[27]:

$$SB_{2q}(t) \approx \cos(2\omega_{IR}t - \Delta\phi_{XUV} - \Delta\phi_{n-e}) \quad (1)$$

where t is the delay between the XUV pump and the IR probe, $\Delta\phi_{XUV}$ represents the additional phase term acquired due to the chirp of the XUV field, $\Delta\phi_{n-e}$ refers to what we name the 'coupled nuclear–electron phase' for our molecular target and ω_{IR} is the fundamental IR frequency.

In the atomic case, this scattering phase is usually called the atomic phase $\Delta\phi_{at}$ and has been unanimously defined as the sum of two contributions: the Wigner scattering phase, that is, the phase difference acquired by the escaping electron subject to a short-range Coulomb potential with respect to a free electron with the same kinetic energy[43], and the continuum–continuum phase term due to the additional IR-induced electronic transitions[5]. The definition of the photoionization time delay is derived from the atomic phase as follows:

$$\tau_{at} = \hbar \frac{\partial\phi_{at}}{\partial E} \cong \hbar \frac{\Delta\phi_{at}}{\Delta E} \quad (2)$$

where $\hbar$ is Plank's constant divided by 2π. In the molecular case, one needs to take into account the influence of the nuclear motion, which in the case of H_2 and the photon energy range considered in this work, happens to be as fast as the electronic motion. Furthermore, the nuclear contribution to the total phase extracted from the oscillating SBs is likely to be state dependent. This implies that to describe the SB amplitude modulation, we need to consider all the intermediate molecular states explicitly depending on both electron and nuclear coordinates.

To clearly visualize the impact of such electron–nuclear coupling on the resulting phase $\Delta\phi_{n-e}$, we built a 3D phase–time map, which shows the behaviour of the extracted spectral phases as a function of both the electron kinetic energy and the KER (Fig. 3). We divided the KER spectrum into intervals of 1 eV and filtered out the RABBITT traces selecting only those corresponding electrons.

In the RABBITT technique, we cannot access the absolute scattering phase of the photoelectrons, as it is unknown when the XUV initiates the photoemission dynamics[5–10,12,13,16,20]. This means that we can only access relative phases defined as follows:

$$\Delta\phi_{2q} = (\phi_{2q}^{intKER} - \phi_{2q}^{1eV-KER}) \quad (3)$$

where ϕ_{2q}^{intKER} and $\phi_{2q}^{1eV-KER}$ are the phases extracted from the fit of the SB of order $2q$ for RABBITT traces composed of photoelectrons corresponding to a KER integrated and 1 eV − KER interval, respectively. It follows that $\Delta\phi_{2q}$ is free from XUV chirp as the $\Delta\phi_{XUV}$ term cancels out. To isolate the dominant contribution of the two populated DESs of different symmetry, we further select the molecular orientation: $\beta_{//}$ and $\beta_\perp$.

Figure 3a shows a 3D map of the experimental relative phases for the perpendicular case $\phi_{2q}^{\beta_\perp}$. There is a clear modulation as a function of both electronic and nuclear energy, becoming more pronounced as the KER increases. It is worth noticing that modulations in the low-KER front corner of Fig. 3a (KER < 3 eV versus all electron energies) can only be associated with the nuclear–electronic coupling, as we can exclude any Q_2 DES contribution in this region (KER + electron energy is below the Q_2 threshold, 31 eV). In contrast, oscillations in the high-KER back corner of Fig. 3a (KER > 3 eV versus all electron energies) are mainly due to autoionization from the Q_2 DES. The relative spectral phases can be converted to photoionization time delays according to the following equation:

$$\Delta\tau_{2q} = \frac{\Delta\phi_{2q}}{2\omega_{IR}} = \frac{(\phi_{2q}^{intKER} - \phi_{2q}^{1eV-KER})}{2\omega_{IR}} \quad (4)$$

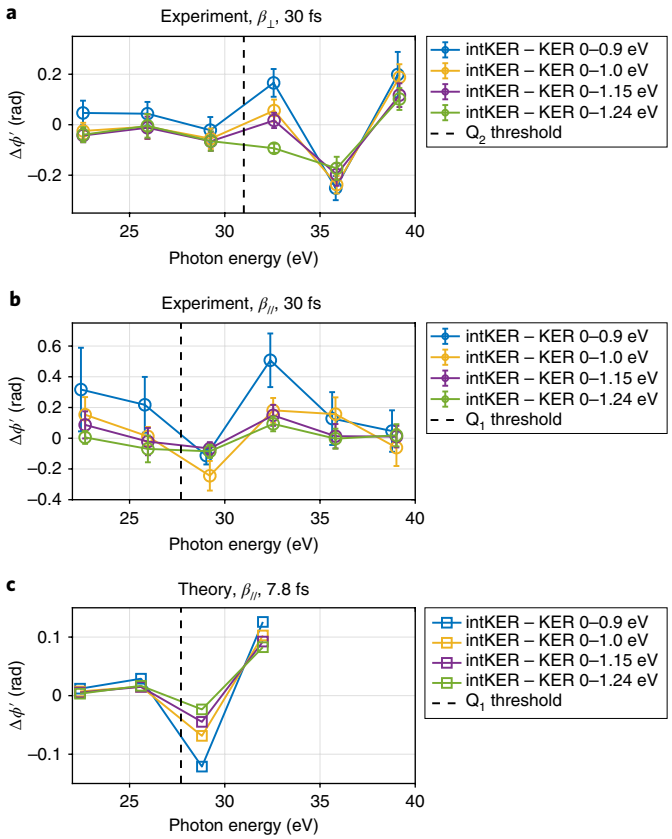

Fig. 4 | Relative molecular phases as a function of the photon energy. **a**,**b**, Experimental data corresponding to $\beta_\perp$ (**a**) and $\beta_{//}$ (**b**). Each experimental data point represents the weighted mean over a set of eight independent measurements. Weighted mean and error bars are calculated considering both the statistical standard deviation over all independent measurements and the average uncertainty of each SB fit as reported in ref. [12]. The smaller error bars in **a** compared with those in **b** are due to better statistics obtained with the higher dissociation probability for the perpendicular orientation (see Fig. 1b). **c**, Ab initio calculations accounting for all interaction terms reproducing the experimental parallel case. The *y*-axis range has been adapted to emphasize the trend. The black dashed lines indicate the Q_2 (**a**) and Q_1 (**b**,**c**) DES energy at the neutral equilibrium distance.

offering a rough but intuitive picture of the dynamics occurring during the molecular dissociation process. If the escaping electron was not affected by the nuclear dynamics taking place during the photoionization and dissociation processes, $\Delta\tau_{2q}$ should strictly be zero, as the electron feels the same molecular potential irrespective of any KER selection. Obviously, this is not the case when resonances are involved, for example, in the vicinity of the Q_1 and Q_2 DES, as the nuclei have enough time to move before autoionization occurs, so that the electron feels a different molecular potential at the instant of ejection. However, we also see that $\Delta\tau_{2q}$ can be different from zero in the non-resonant region. According to equation (4), this can only be associated with the KER selection, that is, to a specific nuclear dynamics, which is thus able to slow down (positive delay) or accelerate (negative delay) the photoemitted electrons. As can be observed, the relative time delays span from −400 as (blue) to above +300 as (red). The experimental 3D map for the parallel case could not be obtained due to the limited statistics at KER > 2 eV in this configuration. Nevertheless, we could benefit from the ab initio calculations to reproduce the relative phases for the parallel case $\Delta\phi_{2q}^{\beta_{//}}$ and strengthen our conclusions. Figure 3b shows the 3D map of the theoretical $\Delta\phi_{2q}^{\beta_{//}}$, which shows the same trend as in Fig. 3a, meaning that $\Delta\phi_{2q}^{\beta_{//}}$ is clearly dependent not only on the electron energy but also on the nuclear kinetic energy, especially where the Q_1 DES does not contribute (KER < 3 eV).

The large modulation in the measured and calculated delays is the consequence of the interplay between non-resonant and resonant photoelectron emission, as well as dissociation. For the first two processes, a similar modulation of delays has been predicted both theoretically[44] and experimentally[9] in the vicinity of autoionizing states of atoms. This has led to a re-interpretation of the relation between the concepts of photoemission delays and Wigner delays[9,44]. The main difference here is that the active role played by dissociation makes this picture even richer. In addition to the ionization time delay, an equivalent 'dissociation time delay' could be defined at a given electron kinetic energy from an expression similar to that given in equation (2), but written now in terms of a KER derivative instead of an electron energy derivative. Not surprisingly, variations in the dissociation time delays at a given electron energy can be as large as those observed in the ionization time delays at a given KER (Fig. 3).

For a more direct comparison between measured and calculated delays, and to further emphasize the impact of autoionization and dissociation processes on the overall dynamics, we defined a different relative phase as $\Delta\phi'_{2q} = (\phi_{2q}^{\mathrm{intKER}} - \phi_{2q}^{\mathrm{lowKER}})$, where $\Delta\phi_{2q}^{\mathrm{lowKER}}$ is the phase of SB_{2q} selected on a low-KER region ranging from 0 eV to a variable upper bound. The low-KER region was chosen to span from 0.9 to 1.24 eV, where the bond-softening effect plays a significant role. The upper limits of the low-KER intervals correspond to the actual eigenvalues resulting from the diagonalization of the nuclear Hamiltonian in the calculation box and are compatible with our experimental KER resolution (0.05 eV, see Supplementary Information).

Using $\Delta\phi'$ we can now present experimental data for both molecular orientations, $\beta_\perp$ (Fig. 4a) and $\beta_{//}$ (Fig. 4b), and compare the parallel case with the theoretical values (Fig. 4c). As in this case we are analysing KER integrated data, the $\beta_{//}$ integration angle has been reduced to ±10° for a better comparison with the theory.

It is evident that as the low-KER upper bound goes from 0.9 towards 1.24 eV (Fig. 4b), the $\Delta\phi'^{\beta_{//}}_{2q}$ profile becomes smoother and the error bars narrower. Regarding the specific profile of the $\Delta\phi'^{\beta_{//}}_{2q}$ as a function of photon energy, there is a clear feature in the energy range 29–32 eV, in contrast to the other energy poin ts, which appear relatively flat within the error bars. This behaviour is nicely reproduced by our calculations as shown in Fig. 4c and mainly associated with the influence of the Q_1 DES. Nevertheless, the phase variation observed in the experiment is larger than that obtained by theory. This may be due to (1) the short duration of the pulse used in the calculations, which prevents one from accounting for bond-softening effects appearing at low KER (Fig. 2g), or (2) the fact that theory provides information for molecules that are strictly parallel to the polarization direction, while the experimental data are retrieved for molecules contained within an angular cone.

Figure 4a shows the experimental data for the perpendicular configuration where two features can be clearly recognized: first, below 30 eV all curves overlap within the error bars, independent of the choice of the low-KER reference. Second, above 30 eV, the remarkable oscillations flatten as the low-KER upper bound increases. At photon energies above the Q_2 threshold, the relative phase presents a significant phase jump due to the effective population of Q_2 DESs and subsequent autoionization. For photon energies below such threshold, a completely flat profile is expected. Therefore, we conclude that the residual modulation observed in the experimental data is only attributable to the nuclear–electronic coupling. This means that the movement of the nuclei modulates the spectral phase of the escaping electron in the dissociative ionization processes.

To conclude, we have shown that whenever light atoms are involved in the molecular ionization process, the variations of the ionization phases with the nuclear kinetic energy can be as large as variations

with the electron kinetic energy, implying that the outgoing electron wave packet cannot be disentangled from the nuclear wave packet. This suggests that the concept of Wigner time delays widely employed to provide temporal information on the ionization dynamics could be extended to provide similar information on the dissociation dynamics of the remaining cation by analysing the variation of the measured phases with nuclear kinetic energy at fixed photoelectron energy. Therefore, this twofold dependency requires us to reconsider the physical meaning of photoionization time delays, not only in the simple H_2 molecular case, but also in most organic and biologically relevant molecules containing light atoms. Furthermore, the present study represents the first attempt towards a full reconstruction of the complete molecular wave packet, thus opening the way to control its dynamics.

Methods

Methods, including statements of data availability and any associated accession codes and references, are available at https://doi.org/10.1038/s41567-018-0103-2.

Received: 6 October 2017; Accepted: 7 March 2018;
Published online: 16 April 2018

References

1. Hentschel, M. et al. Attosecond metrology. *Nature* **414**, 509–513 (2001).
2. Sansone, G. et al. Isolated single-cycle attosecond pulses. *Science* **314**, 443–446 (2006).
3. Eckle, P. et al. Attosecond ionization and tunneling delay time measurements in helium. *Science* **322**, 1525–1529 (2008).
4. Schultze, M. et al. Delay in photoemission. *Science* **328**, 1658–1662 (2010).
5. Klünder, K. et al. Probing single-photon ionization on the attosecond time scale. *Phys. Rev. Lett.* **106**, 143002 (2011).
6. Månsson, E. P. et al. Double ionization probed on the attosecond timescale. *Nat. Phys.* **10**, 207–211 (2014).
7. Guenot, D. et al. Measurements of relative photoemission time delays in noble gas atoms. *J. Phys. B* **47**, 245602 (2014).
8. Palatchi, C. et al. Atomic delay in helium, neon, argon and krypton. *J. Phys. B* **47**, 245003 (2014).
9. Kotur, M. et al. Spectral phase measurement of a Fano resonance using tunable attosecond pulses. *Nat. Commun.* **7**, 10566 (2016).
10. Jordan, I. et al. Spin-orbit delays in photoemission. *Phys. Rev. A* **95**, 013404 (2017).
11. Sabbar, M. et al. Resonance effects in photoemission time delays. *Phys. Rev. Lett.* **115**, 133001 (2015).
12. Cattaneo, L. et al. Comparison of attosecond streaking and RABBITT. *Opt. Express* **24**, 29060–29076 (2016).
13. Haessler, S. et al. Phase-resolved attosecond near-threshold photoionization of molecular nitrogen. *Phys. Rev. A* **80**, 011404 (2009).
14. Sansone, G. et al. Electron localization following attosecond molecular photoionization. *Nature* **465**, 763–766 (2010).
15. Calegari, F. et al. Ultrafast electron dynamics in phenylalanine initiated by attosecond pulses. *Science* **346**, 336–339 (2014).
16. Huppert, M., Jordan, I., Baykusheva, D., von Conta, A. & Wörner, H. J. Attosecond delays in molecular photoionization. *Phys. Rev. Lett.* **117**, 093001 (2016).
17. Remacle, F. & Levine, R. D. An electronic time scale in chemistry. *Proc. Natl Acad. Sci. USA* **103**, 6793–6798 (2006).
18. Vibok, A. & Balint-Kurti, G. G. Parametrization of complex absorbing potentials for time-dependent quantum dynamics. *J. Phys. Chem.* **96**, 8712–8719 (1992).
19. Cavalieri, A. L. et al. Attosecond spectroscopy in condensed matter. *Nature* **449**, 1029–1032 (2007).
20. Locher, R. et al. Energy-dependent photoemission delays from noble metal surfaces by attosecond interferometry. *Optica* **2**, 405–410 (2015).
21. Bandrauk, A. D., Chelkowski, S. & Nguyen, H. S. Attosecond localization of electrons in molecules. *Int. J. Quant. Chem.* **100**, 834–844 (2004).
22. Calvert, C. R., Bryan, W. A., Newell, W. R. & Williams, I. D. Time-resolved studies of ultrafast wavepacket dynamics in hydrogen molecules. *Phys. Rep.* **491**, 1–28 (2010).
23. Ranitovic, P. et al. Attosecond vacuum UV coherent control of molecular dynamics. *Proc. Natl Acad. Sci. USA* **11**, 912–917 (2014).
24. Lara-Astiaso, M. et al. Decoherence, control and attosecond probing of XUV-induced charge migration in biomolecules. A theoretical outlook. *Faraday Discuss.* **194**, 41–59 (2016).
25. Vacher, M., Bearpark, M. J., Robb, M. A. & Malhado, J. P. Electron dynamics upon ionization of polyatomic molecules: coupling to quantum nuclear motion and decoherence. *Phys. Rev. Lett.* **118**, 083001 (2017).
26. Muller, H. G. Reconstruction of attosecond harmonic beating by interference of two-photon transitions. *Appl. Phys. B* **74**, S17–S21 (2002).
27. Paul, P. et al. Observation of a train of attosecond pulses from high harmonic generation. *Science* **292**, 1689–1692 (2001).
28. Ullrich, J. et al. Recoil-ion and electron momentum spectroscopy: reaction-microscopes. *Rep. Prog. Phys.* **66**, 1463–1545 (2003).
29. Dörner, R. et al. Cold target recoil ion momentum spectroscopy: a 'momentum microscope' to view atomic collision dynamics. *Phys. Rep.* **330**, 95–192 (2000).
30. Sabbar, M. et al. Combining attosecond XUV pulses with coincidence spectroscopy. *Rev. Sci. Instrum.* **85**, 103113 (2014).
31. Wickenhauser, M., Burgdörfer, J., Krausz, F. & Drescher, M. Time resolved Fano resonances. *Phys. Rev. Lett.* **94**, 023002 (2005).
32. Sanz-Vicario, J. L., Bachau, H. & Martin, F. Time-dependent theoretical description of molecular autoionization produced by femtosecond XUV laser pulses. *Phys. Rev. A* **73**, 033410 (2006).
33. Kling, M. F. et al. Control of electron localization in molecular dissociation. *Science* **312**, 246–248 (2006).
34. Palacios, A., Sanz-Vicario, J. L. & Martín, F. Theoretical methods for attosecond electron and nuclear dynamics: applications to the H_2 molecule. *J. Phys. B* **48**, 242001 (2015).
35. Lafosse, A. et al. Molecular frame photoelectron angular distributions in dissociative photoionization of H_2 in the region of the Q_1 and Q_2 doubly excited states. *J. Phys. B* **36**, 4683–4702 (2003).
36. Martín, F. et al. Single photon-induced symmetry breaking of H_2 dissociation. *Science* **315**, 629–633 (2007).
37. Sánchez, I. & Martín, F. Resonant dissociative photoionization of H_2 and D_2. *Phys. Rev. A* **57**, 1006–1017 (1998).
38. Ito, K., Hall, R. I. & Ukai, M. Dissociative photoionization of H_2 and D_2 in the energy region of 25–45 eV. *J. Chem. Phys.* **104**, 8449–8457 (1996).
39. Palacios, A., Feist, J., González-Castrillo, A., Sanz-Vicario, J. L. & Martín, F. Autoionization of molecular hydrogen: where do the Fano lineshapes go? *Chem. Phys. Chem.* **14**, 1456–1463 (2013).
40. Bucksbaum, P. H., Zavriyev, A., Muller, H. G. & Schumacher, D. W. Softening of the H_2^+ molecular bond in intense laser fields. *Phys. Rev. Lett.* **64**, 1883–1886 (1990).
41. Zavriyev, A., Bucksbaum, P. H., Muller, H. G. & Schumacher, D. W. Ionization and dissociation of H_2 in intense laser fields at 1.064 µm, 532 nm, and 355 nm. *Phys. Rev. A* **42**, 5500–5513 (1990).
42. Giusti-Suzor, A., Mies, F. H., DiMauro, L. F., Charron, E. & Yang, B. Dynamics of H_2^+ in intense laser fields. *J. Phys. B* **28**, 309–339 (1995).
43. Wigner, E. P. Lower limit for the energy derivative of the scattering phase shift. *Phys. Rev.* **98**, 145–147 (1955).
44. Argenti, L. et al. Control of photoemission delay in resonant two-photon transitions. *Phys. Rev. A* **95**, 043426 (2017).

Acknowledgements

This work is supported by the European Research Council (ERC) advanced grants ERC-2012-ADG_20120216 and ERC with grant agreement 290853 XCHEM within the Seventh Framework Programme of the European Union. We also acknowledge the financial support from the Ministry of Economy and External Trade (MINECO) projects FIS2013-42002-R and FIS2016-77889-R, and the European COST Action XLIC CM1204, and the computer time from the Centro de Computación Científica-Universidad Autónoma de Madrid (CCC-UAM) and Marenostrum Supercomputer. A.P. acknowledges a Ramón y Cajal contract from the Ministerio de Economiía y Competitividad (Spain). F.M. acknowledges support from the 'Severo Ochoa' Programme for Centres of Excellence in R&D (MINECO, Grant SEV-2016-0686) and the 'María de Maeztu' Programme for Units of Excellence in R&D (MDM-2014-0377).

Author contributions

L.C., J.V., L.P. and S.H. performed the experimental measurements. L.C. and J.V. performed the experimental data analysis. R.Y.B., A.P. and F.M. performed the theoretical calculations and analysis. L.C., J.V., M.L., C.C., R.B., A.P., F.M. and U.K. contributed to the data interpretation, scientific discussion and to the manuscript.

Competing interests

The authors declare no competing interests.

Additional information

Supplementary information is available for this paper at https://doi.org/10.1038/s41567-018-0103-2.

Reprints and permissions information is available at www.nature.com/reprints.

Correspondence and requests for materials should be addressed to L.C.

Publisher's note: Springer Nature remains neutral with regard to jurisdictional claims in published maps and institutional affiliations.

Methods

Experimental details. The XUV pump was generated by focusing a strong, linearly polarized IR field (central wavelength 780 nm) into an Ar gas target resulting in an APT centred at 35 eV, which only comprises odd multiples $2q+1$ of the fundamental IR frequency ω_{IR}, as shown in Fig. 1c. The probe pulse, in contrast, is a weak IR pulse exhibiting a peak intensity of between 1.4×10^{11} and 3.0×10^{11} W cm^{-2} and a pulse duration of roughly 30 fs.

In the presented experiments, the focused XUV pump on a cold H_2 gas jet induces single-photon transitions. As a consequence, H_2 molecules ionize and dissociate with a total kinetic energy corresponding to the photon energy minus the H_2 ionization potential, I_p, that is, $E_{tot}=(2q\pm1)\times\hbar\omega_{IR}-I_p$, where q is an integer number, forming HHs ($HH_{2q\pm1}$), as indicated by the blue arrows in Fig. 1c,e.

Each RABBITT spectrogram is obtained by collecting the photoelectron spectrum integrated over all ionic fragments (H_2^+ and H^+), β angle and KER. Each pump–probe delay point is integrated for 3,600 s (10 kHz laser repetition rate). The delay point spacing is about 0.2 fs (see Fig. 1e). Regarding the detection of photoelectrons, we consider in the data analysis a selection cone with an aperture of ±60° with respect to the XUV polarization axis.

The backpressure used for the H_2 cold jet was 1.4 bar, to maintain the lowest possible count rate on both ion and electron detectors, thus to avoid false coincidences. In particular, the count rates on the ion and electron time-of-flight signals were 0.8 and 1.6 KHz, respectively.

Quantum paths description involving the DESs. The Q_1 states can be accessed on absorption of XUV photon energies in the range 25–30 eV for molecules preferentially oriented along the XUV polarization axis. This means that only parallel transitions can significantly populate the Q_1 DESs followed by autoionization, leaving the molecular cation in its $^2\Sigma_g^+(1s\sigma_g)$ ground state. The resulting ion fragments after dissociation will appear with KER between 1 and 10 eV (refs [37,38,45,46]). The Q_2 DESs are instead excited by XUV photons with $E_{XUV}>31$ eV, mostly for molecules oriented orthogonally to the XUV polarization axis. The Q_2 states can then autoionize to both $^2\Sigma_g^+(1s\sigma_g)$ and $^2\Sigma_u^+(2p\sigma_u)$ states of the cation that can later dissociate with KER 1–5 eV and 5–8 eV, respectively[47].

Ab initio calculations. We have solved the time-dependent Schrödinger equation in full dimensionality using the spectral method described in ref. [34] and successfully employed to describe XUV pump–IR probe scheme in single ionization of hydrogen molecules[14,23,34]. The time-dependent wave function was expanded in a basis set of Born–Oppenheimer states in which the electronic components are built as antisymmetrized products of H_2^+ states and one-electron continuum wave functions resulting from an L^2 close-coupling solution of the scattering equations. These continuum wave functions are expanded in a basis of products of spherical harmonics (for the angular part) and B-spline functions (for the radial part). To properly describe the relatively long interaction times of the electrons with the combined XUV and IR fields, we employed a particularly large radial box to define the B-spline basis, namely 300 a.u., and a maximum angular momentum of $l_{max}=11$. At a photon energy of 32 eV, a typical value in the present experiment, electrons are emitted with a kinetic energy of around 14 eV, which implies that they take around 6–7 fs to reach the box boundary. For pulses longer than that, electrons ejected during the earlier cycles may be artificially reflected at the box boundary while other electrons are still being ionized by the later cycles, thus leading to unphysical interferences in the photoelectron spectrum. Therefore, to ensure numerical stability, which is particularly relevant when looking at relative phases resulting from continuum–continuum dipole transitions, we have limited the duration of the IR pulse and the associated APT to 7.8 fs (see Supplementary Information). The nuclear components have been obtained by diagonalizing, for each electronic state, the corresponding nuclear vibrational Hamiltonian in a basis of B-spline functions defined in a box of 12 a.u. This box is large enough to avoid unphysical reflections of the dissociating nuclei during the interaction with the pulse. We computed photoionization amplitudes for molecules oriented parallel to the polarization direction, so that the XUV APT can only induce transitions from the $X\,^1\Sigma_g^+$ (vibrational state quantum number $v=0$) ground state to the $^1\Sigma_u^+$ continuum and the subsequent IR pulse from the latter to the $^1\Sigma_g^+$ continuum. We have included all continuum states associated with the two lowest ionization thresholds, that is, the $^2\Sigma_g^+(1s\sigma_g)$ and $^2\Sigma_u^+(2p\sigma_u)$ states of H_2^+, which are the only ones that can be significantly accessed in the present experiment[48].

Data availability. The data that support the plots within this paper and other findings of this study are available from the corresponding author upon reasonable request.

References

45. Sánchez, I. & Martín, F. The doubly excited states of the H_2 molecule. *J. Chem. Phys.* **106**, 7720–7730 (1997).
46. Latimer, C. J., Irvine, A. D., McDonald, M. A. & Savage, O. G. The dissociative photoionization of hydrogen via two-electron excitation at 27.5 eV and 30.5 eV. *J. Phys. B* **25**, L211–L214 (1992).
47. Sánchez, I. & Martín, F. Dissociative photoionization of H_2 and D_2 by (30–37)-eV photons via $^1\Pi_u$ states. *Phys. Rev. A* **60**, 2200–2206 (1999).
48. Aoto, T. et al. Dissociative photoionization of H_2 at high photon energies: uncovering new series of doubly excited states. *Chem. Phys. Lett.* **389**, 145–149 (2004).